Applied Surface Science 542 (2021) 148665

Contents lists available at ScienceDirect

Applied Surface Science

journal homepage: www.elsevier.com/locate/apsusc

Full Length Article

Highly anisotropic electronic and mechanical properties of monolayer and bilayer As_2S_3

Xuefei Liu [a,b], Zhaofu Zhang [c], Zhao Ding [b], Bing Lv [a], Zijiang Luo [d], Jian-Sheng Wang [e], Zhibin Gao [e]

[a] Key Laboratory of Low Dimensional Condensed Matter Physics of Higher Educational Institution of Guizhou Province, Guizhou Normal University, Guiyang 550025, China
[b] Low-Dimensional Semiconductor Structure Laboratory, College of Big data and Information Engineering, Guizhou University, Guiyang 550025, China
[c] Department of Engineering, University of Cambridge, Cambridge CB2 1PZ, United Kingdom
[d] College of Information, Guizhou University of Finance and Economics, Guiyang 550025, China
[e] Department of Physics, National University of Singapore, Singapore 117551, Republic of Singapore

ARTICLE INFO

Keywords:
2D arsenic trisulfide (As_2S_3)
Ab initio calculations
Anisotropy
Electronic structure
Effective mass
Mechanical properties

ABSTRACT

Two-dimensional(2D) material with high anisotropy as well as robust stability would inspire significant interest in the new-generation electronic and optomechanical field, especially for directional memories, synaptic, neuromorphic and polarization-sensitive photodetector devices. Recently, 2D As_2S_3 was successfully exfoliated in experiments (Šiškins et al., 2019) and was demonstrated to be stable in the ambient. Herein, by using first principles method, we further systematically predicted its angular-dependent electronic and mechanical properties. Specifically, the angle-resolved effective mass of carriers, carrier mobility, three dimensional band structure, stress–strain relationships, as well as the angle-dependent mechanical properties are investigated. Our results show that 2D As_2S_3 owns a high anisotropic nature both electronically and mechanically. We found that, due to the large anisotropic charge distributions, 2D single (bilayer) As_2S_3 has shown a value of 3.15 (3.32) in Young's modulus ratio along two axes. These values are much greater than the corresponding 2D black phosphorous of 2 (Tao et al., 2015), which is experimentally confirmed the largest one up to date. Our findings provide an valuable avenue to realize the flexible orientation-dependent nano-devices.

1. Introduction

Many materials are anisotropic and even inhomogeneous owning to the tunable formation and composition of their constituents and elements. Currently, large amount of two-dimensional (2D) materials including graphene [3,4], h-BN [5], transition metal dichalcogenides [6,7] are found to be isotropic. During the past years, some 2D structures were demonstrated with limited anisotropy. Such as SnSe [8], and atomically thin tellurium [9,10]. Besides, although black phosphorus [11] was found to be a highly anisotropic 2D material, the weak stability seriously constraint its practical applications. Most glasses and polymers are examples of isotropic materials, which have been widely used in the packaging industry, medical equipment, and even home tableware. On the contrary, the properties of anisotropic materials are direction-dependent, which usually consists of asymmetric crystalline structures. Furthermore, artificial anisotropic single crystals (metamaterials) are also highly desired as developing technology, such as selective fluorescence DNA sensors [12], anisotropic synaptic devices for neuromorphic applications [13], anisotropic nanoelectronics with multifunctional directional memories in the 2D limit [14], digital inverters [15], and even polarization-sensitive broadband photodetectors [16].

Recently, low-symmetry monolayer and few-layer materials have appeared on the stage owing to the unique orientation-dependent properties that are not easily obtained in the usual isotropic and symmetric 2D materials [17–21,2]. In these anisotropic 2D materials, the electronic, optical, thermal, piezoelectric, and even ferroelectric properties are direction-dependent, which would open up more potential to selectively harness the physical properties of 2D materials-based nanodevices [22,15,23,14,24]. At present, 2D black phosphorus (BP) was reported having a large value of $\frac{E_b}{E_a} = 2$ in Young's modulus [2,25]. BP, yet, has a fatal disadvantage that is unstable in the ambient conditions, which severely constrains its potential applications [26].

Past year, free-standing 2D As_2S_3 with robust atmospheric stability was exfoliated successfully in the experiment by Šiškins et al. [1] and

E-mail address: zhibin.gao@nus.edu.sg (Z. Gao).

https://doi.org/10.1016/j.apsusc.2020.148665
Received 15 September 2020; Received in revised form 16 November 2020; Accepted 30 November 2020
Available online 13 December 2020

they have also systematically studied the anisotropic optical properties such as Raman spectroscopy, resonance frequency analysis using laser interferometry [1]. However, both the mechanical and electronic anisotropic character of 2D As_2S_3 is still unclear yet. Is the anisotropy of a single (bilayer) layer greater than that of a multi-layer in As_2S_3? How does the anisotropy of monolayer and bilayer As_2S_3 compare to the well-known BP?

Herein, we have systematically explored the anisotropic properties of 2D As_2S_3 using first-principle methods, mainly focusing on the electronic and mechanical properties. Furthermore, we have elaborately analyzed the angle-resolved effective mass of holes and electrons, angle-resolved Young's modulus, Poisson's ratio and Shear modulus of monolayer and bilayer As_2S_3. The calculated anisotropic factor of monolayer and bilayer As_2S_3 are 3.15 and 3.32 respectively, which are quite larger than the renowned BP with an anisotropic ratio of 2. Our studies will provide a more comprehensive understanding and insights into the potential applications of 2D As_2S_3 in orientation-dependent nanoscience and nanotechnology.

2. Computational methods

The optimization of structures and static self-consistent energy calculations were conducted using the PBE functional [27]. We optimized materials and calculated band structures in vasp code [28,29]. The energy cutoff is 400 eV. We use a $4 \times 12 \times 1$ Monkhorst–Pack k-point to sample the reciprocal space. The energy and force on each atoms criterion are 10^{-5} eV and 0.02 eV/Å. Van der Waals (vdW) dynamical correlations was also considered by the DFT-D2 method of Grimme [30], a correction to the conventional Kohn–Sham DFT energy. A vacuum thickness with 20 Åwas used. To describe a more accurate band structure, we used HSE06 [31]. The angle-resolved effective mass of holes and electrons, angle-resolved mechanical properties were performed using VASPKIT code [32].

3. Results and discussions

3.1. Crystal structure and anisotropic charge distribution

The optimized crystal structures of 2D monolayer and bilayer As_2S_3 in a 2×2 supercell are shown in Fig. 1. The stability of 2D monolayer As_2S_3 has been checked in our previous study [33]. However, it is noted that the excited state induced by excessive light would convert the structure of As_2S_3 into an amorphous phase, thus affecting the stability of the structure [34]. Monolayer As_2S_3 is the Orthorhombic crystal system with $Pmn2_1$ symmetry group (space group No. 31). The primitive cell of monolayer As_2S_3 contains 10 atoms, highlighted by a black solid rectangle in Fig. 1(a). There are two distinct types of elements in monolayer and bilayer As_2S_3. The hinged S atoms have a coordination number of two, while the rigid As atoms have a coordination number of three. Due to the weak vdW interaction, As_2S_3 can be exfoliated from the bulk counterpart, resulting in a monolayer or layered As_2S_3 Membranes [1]. Therefore, we would like to explore the bilayer As_2S_3 which consists of 20 atoms. Note that the bilayer As_2S_3 remains the same stacking formation with the 3D As_2S_3 phase belonging to the $P2_1/c$ [35], indicating the bilayer can be easily obtained from the 3D As_2S_3. The optimal interlayer intrinsic distance is 2.04 Å based on the DFT-D2 functional, which is a little smaller than the 3D As_2S_3 of 2.79 Å. The optimized lattice constants of the monolayer (bilayer) As_2S_3 are $|\vec{a}| = 11.42$ (11.49) Å and $|\vec{b}| = 4.41$ (4.33) Å, respectively, which are in a good agreement with the previous work [35].

Bader charge is an effective analysis of assigning electron density of molecules and solids to individual atoms [36]. The calculated Bader charge of monolayer, bilayer and three-layer As_2S_3 are shown in Figs. 1 (c), 1(g) and 1(h), respectively. For comparison, red (blue) color represents losing (gaining) electrons, and the depth of each color is used to describe the amount of charge transfer. Based on our calculation, each arsenic atom loses an average of 0.27 e (0.46 e) electrons for monolayer

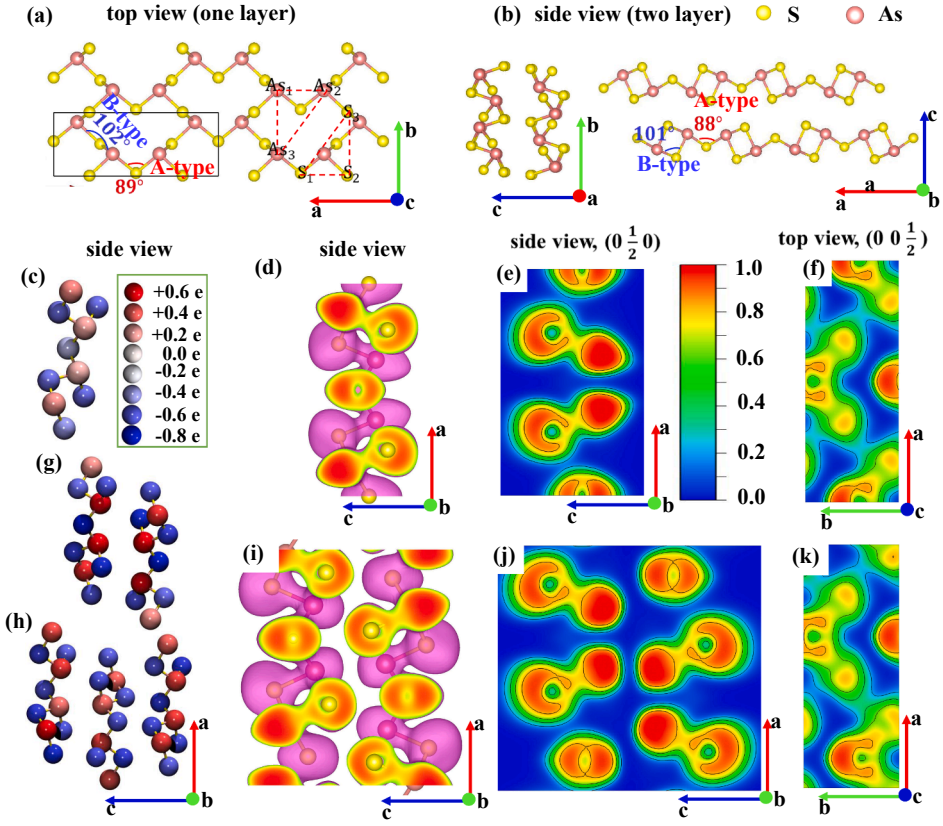

Fig. 1. (a)(b) Top and side views of the monolayer and bilayer 2D As_2S_3 in a 2×2 supercell. The primitive cell of monolayer As_2S_3 is indicated by a solid black rectangle. According to the different hinged deformation, the As—S—As bond angles can be classified into two types (A and B), shown in (a) and (b). (c), (g) and (h) depict the Bader charge distribution for monolayer, bilayer and three layer As_2S_3, respectively. (d)-(k) (except for (h)) describe the electron localization function (ELF) for monolayer (above) and bilayer (below) As_2S_3, separately. (d) and (h) are the 3D ELF and the iso-surface value in the side views of ELF is 0.59. The Miller indexes for top views and side views are (0 0 1/2) and (0 1/2 0). The blue and red colors in (c) and (g) represent gaining and losing electrons, and the number of transferred electrons are characterised by the depth of colors. The maximum value of obtaining and losing electrons are shown in (c) and (g). (For interpretation of the references to colour in this figure legend, the reader is referred to the web version of this article.)

and bilayer, respectively. By comparing the depth of red or blue color in Figs. 1(c) and (g), it is also obvious that the number of transferred electrons in the bilayer As_2S_3 is much more than that in monolayer As_2S_3. The different amount of electrons transfer originates from the Van der Waals interaction between the two sub-layers in the bilayer structure. In order to get a clear picture of the change, we further calculated the Bader charge for three-layer As_2S_3, as shown in Fig. 1(h). As expected, the Bader charge feature is very similar to that of the bilayer case. The average transfer electrons from the arsenic atom to the sulphur atom are 0.43 *e*, which is approximate to that of the bilayer. Besides, the different color distributions of Bader charge along $\vec{a}$ and $\vec{b}$ direction imply the anisotropy of electronic properties in 2D As_2S_3.

Electron localization function (ELF) is another tool to investigate the bonding nature between two atoms [37]. It is a three-dimensional function with a value ranging from 0 that indicates a low electron density localization and metallic ionic bonds to 1 that implies strong covalent bonding or lone pair electrons. The calculated ELF for monolayer As_2S_3 are shown in Figs. 1(e) and 1(f). The result shows that ELF of sulfur atoms is larger than that of arsenic atoms, indicating a large anisotropic charge distribution of monolayer As_2S_3. Figs. 1(j) and 1(k) also depict a similar charge distribution of bilayer As_2S_3 with the monolayer As_2S_3. Furthermore, the strong electron localization locates between sulfur and arsenic atoms, indicating the dominant role of covalent bonding in both monolayer and bilayer As_2S_3.

The Bader charge and ELF can be further explained by the different electronegativity of sulfur (2.58) and arsenic (2.18) atoms. Therefore, sulfur atoms tend to gain more electrons than arsenic atoms due to a larger electronegativity. This covalent bond mechanism in bilayer As_2S_3 is stronger than the monolayer As_2S_3, which can be verified in Figs. 1(e) and 1(j). What is more, Figs. 1(f) and 1(k) display the different electron densities in the 2D plane,no matter in monolayer and bilayer As_2S_3. This outcome demonstrates that electrons are more continuous and denser in the $\vec{a}$ axis compared with the $\vec{b}$ axis, suggesting a large anisotropic charge distribution for monolayer and bilayer As_2S_3. This special electron behavior will lead to the anisotropic properties of As_2S_3. We will discuss it in the following sections.

3.2. Anisotropic electronic transport properties

Next, we study the electronic properties of both monolayer and bilayer As_2S_3. The calculated band structures are shown in Figs. 2(a) and 2(b), indicating indirect semiconductors for monolayer and bilayer As_2S_3. For monolayer, the CBM is occurred at the Γ point while the VBM lies between the Γ and Y point (0 1/2 0), marked as Δ in the 2(a). In the case of the bilayer, the location of CBM changes little but the VBM is transformed to the S point (1/2 1/2 0), due to the weak vdW interaction. Based on the DFT-PBE calculations, the monolayer As_2S_3 has an indirect band gap of 2.17 eV, and the bilayer is 1.97 eV. This is consistent with the physical picture that usually monolayer material has a larger band gap than that of the few-layer material [38].

Considering the fundamental bandgap of As_2S_3 is underestimated in DFT-PBE calculations, we have resorted to the HSE06. The calculated HSE06 band gaps for monolayer and bilayer As_2S_3 are 3.11 and 2.91 eV, respectively. Our monolayer HSE06 band gap is 0.16 eV smaller than the previous work [35] since we used a much dense *k* point to do the calculation. Note that the locations of CBM and VBM are the same as their results [35]. It is also found that the HSE06 method does not change not only the shape of the band structures of monolayer and bilayer As_2S_3, but also for the positions of VBM and CBM (band edges). Besides, the bands shown in Figs. 2(a) at CBM along Γ–X direction are more non-dispersive than that of Γ–Y direction, resulting in a smaller electron effective mass along Γ–X direction. In the case of the bilayer, the band edge along Γ–X direction is much flatter than that of Γ–Y direction, thus, leading to a larger electron effective mass in Γ–X direction. As for the VBM, a similar discussion can be done but is omitted for simplicity. The carrier effective masses at band edges for monolayer and bilayer As_2S_3 along two different directions are listed in Table 1. These results indicate strong electronic anisotropy for monolayer and bilayer As_2S_3, which can be explained by the anisotropic crystal structure, as shown in Fig. 1 (a), the lattice constant in $\vec{b}$ direction is much smaller than that of $\vec{a}$ direction. Besides, as discussed above based on the Bader charge results, the charge distribution is not uniform, thus would induce the anisotropic electronic properties as well. Therefore, we need more quantitative study of electronic transport properties for As_2S_3 systems in the following.

Besides, we also show the atomic projected density of states (PDOS) as well as the charge density distributions of VBM and CBM based on the HSE06 level for monolayer in Fig. 1bilayer in Figs. 3(e), 3(g) and 3(f). Evidently, the PDOS for monolayer and bilayer As_2S_3 show that the VBM is mainly dominated by the *p* orbital of sulfur atoms. On the contrary, the

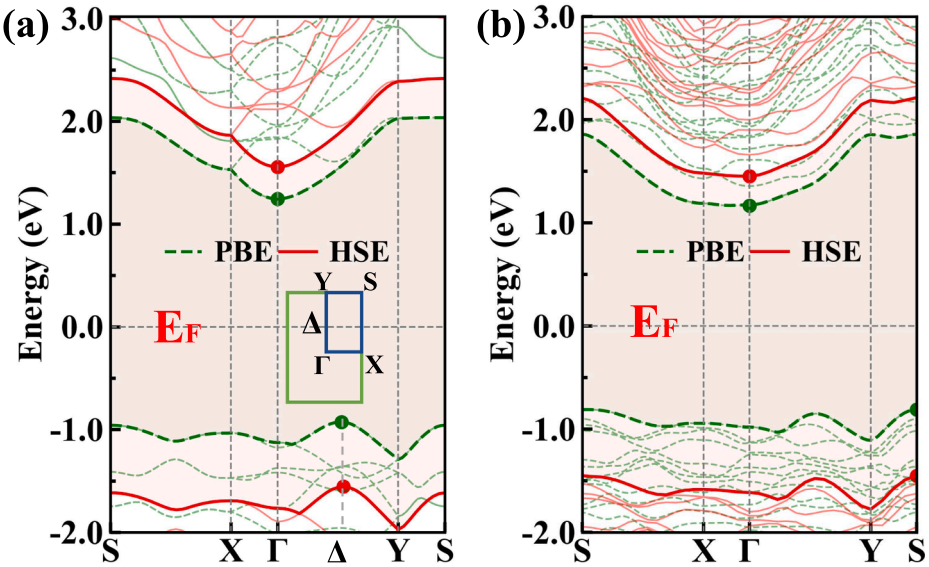

Fig. 2. Electronic band structures of (a) monolayer and (b) bilayer 2D As_2S_3 using the DFT–PBE (dashed green) and DFT-HSE06 (solid red) functionals. The insertion in (a) is the brillouin zone of 2D As_2S_3. The high-symmetry *k* are: S(0.5 0.5 0), X(0.5 0 0), Γ(0 0 0), Δ(0 0.26 0) and Y(0 0.5 0). E_F is the Fermi level. (For interpretation of the references to colour in this figure legend, the reader is referred to the web version of this article.)

Table 1
The elastic modulus(C_x^{2D}, C_y^{2D}), carrier effective mass(m_x^*, m_y^*), the deformation potential(E_1^x, E_1^y) as well as the mobility(μ_x^{2D}, μ_y^{2D}) of 2D As_2S_3 at 300 K.

Structure	Carrier type	$m_x^*(m_0)$ $\Gamma(\Delta,S)$-X	$m_y^*(m_0)$ $\Gamma(\Delta,S)$-Y	E_1^x (eV)	E_1^y (eV)	C_x^{2D} (J/m^2)	C_y^{2D} (J/m^2)	μ_x^{2D} (cm^{2}V^{-1}s^{-1})	μ_y^{2D} (cm^{2}V^{-1}s^{-1})
Monolayer	Electron	0.94	1.04	1.71	1.18	32.13	10.96	253.11	163.78
	Hole	2.24	0.68	4.74	4.48			10.85	13.74
Bilayer	Electron	1.83	1.3	2.49	1.94	67.31	23.31	81.91	66.23
	Hole	4.37	0.48	5.86	5.22			6.61	26.07

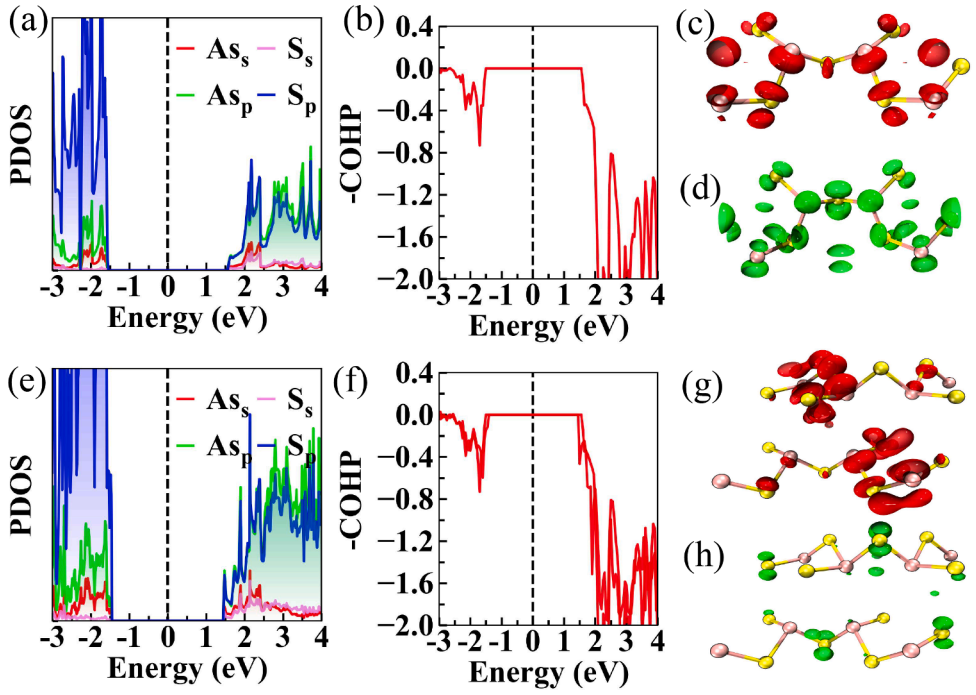

Fig. 3. (a) The atomic projected density of states (PDOS), (b) the crystal orbital hamilton populations(COHP) of monolayer As_2S_3,charge density distributions of (c) CBM and (d) CBM for monolayer As_2S_3. (e)–(h) are the corresponding pictures for bilayer As_2S_3. The Fermi levels are indicated by black dashed lines.

CBM is equally contributed by the *p* orbital of sulfur and arsenic atoms. In order to get a clear picture of the bonding and antibonding nature in the monolayer and bilayer As_2S_3, we further calculated the crystal orbital hamilton populations (COHP) [39], as shown in Figs. 3(b) and 3 (f). The results imply that the CBM and VBM of both monolayer and bilayer As_2S_3 are antibonding states. Combining the PDOS and COHP results, we speculate the VBM may be contributed from antibonding of As-s and S-p states while the CBM may be antibonding by As-p and S-p states.The results are similar to that of 2D SnS_2 [40]. Therefore, we expect our results for effective masses of electrons and holes will further unveil the anisotropic electronic transport in As_2S_3 systems.

To further confirm the anisotropic electronic transport properties, we plot the three-dimensional band structures of monolayer and bilayer As_2S_3, shown in Figs. 4(a) and 4(d), respectively. They demonstrate obvious anisotropic nature at the CBM and VBM. CBM band edges are much more dispersive than that of the VBM band edges, again indicating the strong anisotropic electronic transport properties. The effective mass (in units of electron mass m_0) of carriers at band edges can be calculated by

$$m_i^* = \hbar^2 \left[\frac{\partial^2 E(\mathbf{k_i})}{\partial^2 \mathbf{k_i}} \right]^{-1}, \quad (1)$$

where $E(k_i)$ is the electronic energy dispersion with respect to the electron momentum along *i* (a, b, c) direction. During the process of orientation-dependent effective mass, a uniform *k*–points were sampled along the radial direction at intervals of 10 degrees to calculate the band dispersion relation. Then we fitted the dispersion in a given direction to obtain the angle-dependent effective masses of holes and electrons [32].

Different electronic bands according to the Eq. (1) will result in quantitative effective mass of carriers in different directions. The orientation-dependent effective masses of holes and electrons are depicted in Figs. 4(b) and 4(c) for monolayer and Figs. 4(e) and 4(f) for bilayer As_2S_3 respectively. Obviously, the effective mass of electrons along $\vec{a}$ direction is much smaller than that of in the $\vec{b}$ direction. As for the holes, an opposite trend is found and the anisotropic nature of holes is much stronger than the electrons. These significantly anisotropic transport properties could be beneficial to the separation of electrons and holes which is highly desired in the photovoltaic field [41]. Furthermore, the bilayer As_2S_3 has a larger anisotropic effective masses of holes and electrons compared with the monolayer situation, which will lead to asymmetric transport properties, such as the Seebeck coefficient and electric conductivity and finally potentially enhance the thermoelectric performance [42,43].

In order to give out a clearer understanding about the anisotropy of transport properties, it is necessary to calculate the mobility of electrons and holes in the 2D As_2S_3. Based on the deformation potentials theory proposed by J.Bardeen and W.Shockley [44], the mobility of 2D materials is determined by [45]

$$\mu_{2D} = \frac{e\hbar^3 C_{2D}}{k_B T m^* m_d E_1^2} \quad (2)$$

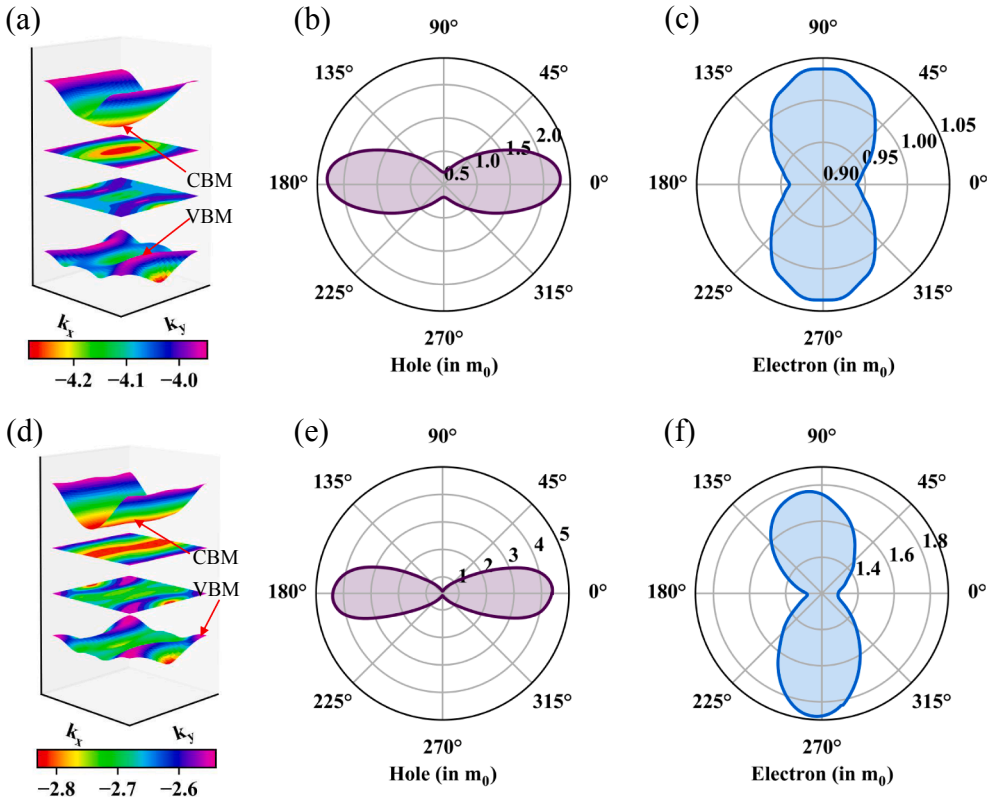

Fig. 4. (a) Three-dimensional (3D) electronic band structure and angle-resolved effective masses of (b) holes and (c) electrons located at VBM and CBM band edges for monolayer As_2S_3. (d)–(f) are the corresponding quantities for bilayer As_2S_3. The CBM and VBM are indicated in (a) and (d).

where the $e, \hbar, C_{2D}, k_B, T$, and m^* are the charge of an electron, reduce Planck's constant, elastic modulus of 2D As_2S_3, Boltzmann constant, thermodynamic temperature, the effective mass of carriers, respectively. m_d is the average effective mass of electron or hole determined by $m_d=\sqrt{m_x^* m_y^*}$ and E_1 denotes the deformation potential constant of the VBM for hole and CBM for electron, calculated by $E_1 = \Delta E/(\Delta l/l_0)$. Here, l_0 and Δl are the lattice constant and the deformation of l_0, separately, and the change step of deformation is 0.5% within a range from -2% to $+2\%$. The mobility as well as other related quantities are summarized in Table 1.

The mobility of electron(hole) for monolayer As_2S_3 in x and y direction is predicted to be 253.11 (10.85) and 163.78 (13.74) $cm^2 V^{-1}s^{-1}$, respectively. As for the bilayer As_2S_3, the corresponding mobility is 81.91 (6.61) and 66.23 (26.07) $cm^2 V^{-1}s^{-1}$, separately. The results show an obviously anisotropic carrier mobility for 2D As_2S_3. Besides, the mobility of holes are much smaller than electrons in both monolayer and bilayer structure, which is beneficial for carrier separation required in the photovoltaic and photocatalytic fields.

3.3. Anisotropic mechanical properties

The mechanical properties of a material are those properties that involve a response to an applied strain, which has wide applications [46–48]. The calculated stress–strain curves of monolayer and bilayer As_2S_3 are shown in Fig. 5, which starts a linear function before the loaded strain is lower than 5%. Above 5%, monolayer and bilayer As_2S_3 enter nonlinear (anharmonic) regions, which are consistent with the previous work [35]. Young's modulus E is the slope in the stress–strain curve locating in the linear region [47]. By fitting calculation, we obtained the elastic modulus for monolayer (bilayer) are 45.4 (85.1) GPa,

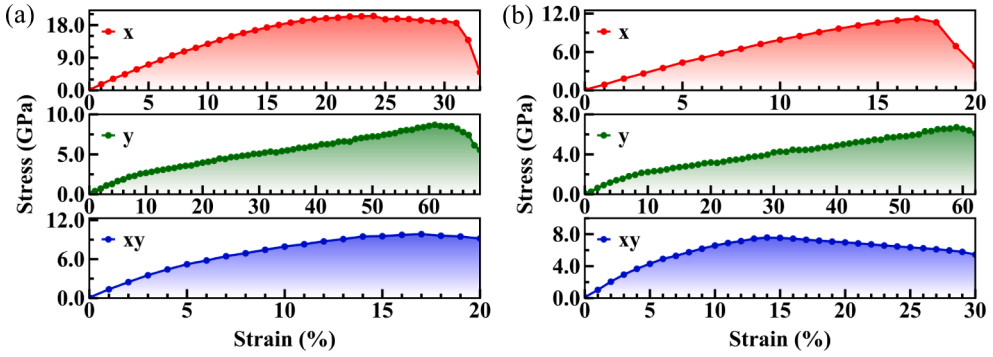

Fig. 5. The relationship between stress and uniaxial/biaxial strain for (a) monolayer and (b) bilayer As_2S_3. In the calculation of uniaxial strain (for example, in the x direction), the lattice constant along x-direction is fixed to a value of L_x, then the lattice constant L_y along the y-axis and the atom positions are optimized until reaching the lowest total energy of the whole system.

and 11.3 (27.4) GPa along with the $x(\vec{a})$ and $y(\vec{b})$ directions, respectively. Due to the rectangle crystals of monolayer and bilayer As_2S_3, the mechanical properties along with x-direction can decouple with the y-direction, which further increases the anisotropic mechanical properties of As_2S_3 systems. This is completely verified by the Figs. 5(a) for monolayer and 5(b) for bilayer As_2S_3.

For a 2D material, the relationship between the stress σ, the in-plane elastic constants tensor C_{ij} (i, j=1,2,6) and strain ε can be correlated based on the Hooke's law under the in-plane stress condition [49,47]

$$\begin{bmatrix} \sigma_{xx} \\ \sigma_{yy} \\ \sigma_{xy} \end{bmatrix} = \begin{bmatrix} C_{11} & C_{12} & 0 \\ C_{12} & C_{22} & 0 \\ 0 & 0 & C_{66} \end{bmatrix} \begin{bmatrix} \varepsilon_{xx} \\ \varepsilon_{yy} \\ 2\varepsilon_{xy} \end{bmatrix} \tag{3}$$

here we use the standard Voigt notation which simplifies the tensor notation into the matrix notation, such as 1–xx, 2–yy, and 6–xy [50]. Besides, since the rectangle crystals of monolayer and bilayer As_2S_3, the elastic constants can be calculated as

$$E_S = \frac{1}{2}C_{11}\varepsilon_1^2 + \frac{1}{2}C_{22}\varepsilon_2^2 + C_{12}\varepsilon_1\varepsilon_2 + 2C_{66}\varepsilon_6^2 \tag{4}$$

where E_S is the strain energy and the tensile strain is defined as $\varepsilon = \frac{L_i - L_{i0}}{L}$ ($i = x, y$). L_i and L_{i0} are the strained and unstrained lattice constants along with x- or y-directions, respectively. To capture the physics, we select the ε_i ($i = 1, 2, 6$) ranging from the -2% to 2% with an increment of 0.5% to calculate the strain energies under different strains for all strained structures, including monolayer and bilayer As_2S_3. Thus the elastic constants can be obtained by fitting the Eq. (4).

To intuitively investigate the mechanical anisotropy of As_2S_3 systems, we calculate the orientation-dependent Young's modulus $E(\theta)$, Poisson's ratio $\nu(\theta)$, and Shear modulus $G(\theta)$ based on [51,52]

$$\begin{aligned} E^{-1} = \; & S_{11}\cos^4\theta + S_{22}\sin^4\theta + 2S_{16}\cos^3\theta\sin\theta \\ & + 2S_{26}\cos\theta\sin^3\theta \\ & + (2S_{12} + S_{66})\cos^2\theta\sin^2\theta, \end{aligned} \tag{5}$$

and

$$-\nu(\theta)/E(\theta) = A + B\cos(4\theta + \psi_1), \tag{6}$$

where

$$A = [(S_{11} + S_{22} - S_{66})/2 + 3S_{12}]/4, \tag{7}$$

$$B = \frac{\sqrt{(S_{26} - S_{16})^2 + [S_{12} - (S_{11} + S_{22} - S_{66})/2]^2}}{4} \tag{8}$$

$$\tan\psi_1 = \frac{S_{26} - S_{16}}{S_{12} - (S_{11} + S_{22} - S_{66})/2}, \tag{9}$$

$$1/4G(\theta) = C + D\cos(4\theta + \psi_2), \tag{10}$$

where

$$C = (S_{11} + S_{22} - 2S_{12} + S_{66})/8, \tag{11}$$

$$D = \frac{\sqrt{(S_{66} + 2S_{12} - S_{11} - S_{22})^2/4 + (S_{26} - S_{16})^2}}{4} \tag{12}$$

$$\tan\psi_2 = \frac{2(S_{16} - S_{26})}{(S_{66} + 2S_{12} - S_{11} - S_{22})}. \tag{13}$$

in which $\theta \in [0, 2\pi]$ is the conventional angle that starts from the $+x$ axis corresponding to the $\theta = 0$. In the experiment, the data of mechanical property sometimes are compliance constants that have a straightforward relation with elastic tensors: S_{ij}=C_{ij}^{-1}. Our calculated results are presented in Figs. 6(a) and 6(c) for monolayer and Figs. 6(d) and 6(f) for bilayer As_2S_3.

At first glance, for bilayer As_2S_3, both Young's modulus E and Poisson's ratio ν decrease to a minimum value then increase as a function of orientation. The maximum and minimum values of E for bilayer are 83 GPa at 0° ($\vec{a}$ axis) and 25 GPa at 90° ($\vec{b}$ axis). The corresponding results of ν are 1.1 and 0.3, respectively. Unfortunately, the situation of monolayer As_2S_3 is complicated where there exist two maximums for E and ν, separately. As for the Shear modulus G, Similar trends can be

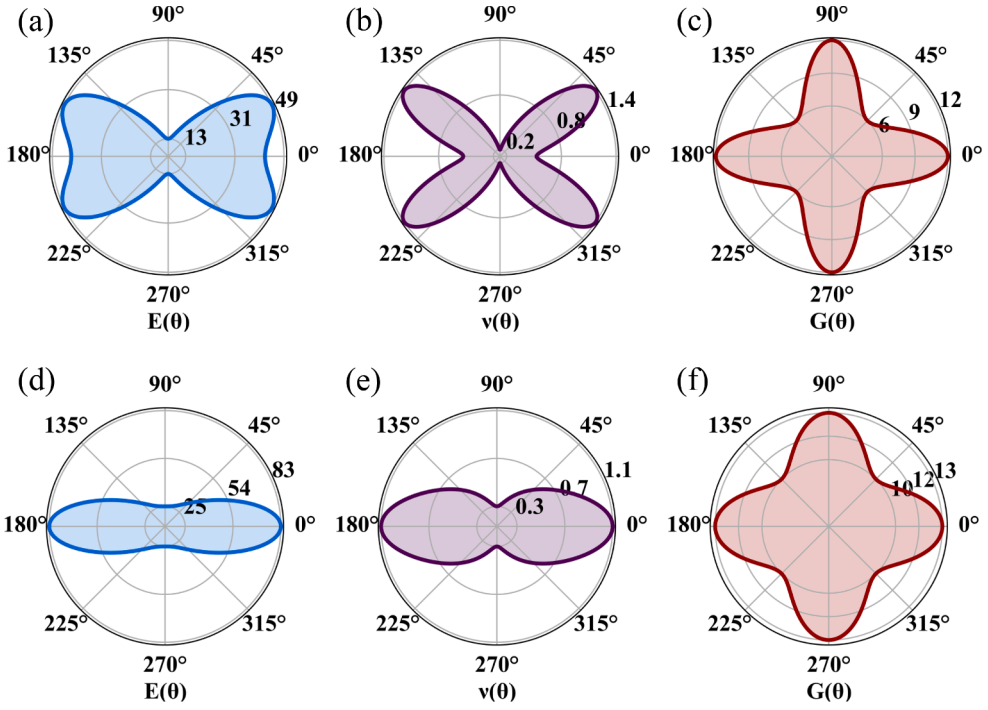

Fig. 6. The calculated angle-resolved Young's modulus $E(\theta)$, Poisson's ratio $\nu(\theta)$, and Shear modulus $G(\theta)$, respectively for (a)–(c) monolayer and (d)–(f) bilayer As_2S_3 according to Eq. (5), (6), and (10).

found for both monolayer and bilayer As_2S_3 shown in Figs. 6(c) and 6(f). The maximum G is around 13 GPa for bilayer, while the minimum G is 10.3 GPa and 5.9 GPa for monolayer and bilayer As_2S_3, respectively.

These results suggest that the anisotropic mechanical properties are obvious both in monolayer and bilayer As_2S_3. What is more, the outcome from the strain–energy method is also verified by Fig. 5, which confirms the correctness and consistency of our computational methods. In our present work, the anisotropic factor of monolayer and bilayer are 3.15 and 3.32, respectively, which is relatively good agreement with the previous experimental measurement [1] and is quite higher than that of BP, confirmed in experiment to be 2 [2].

Furthermore, the absolute value of Young's modulus increases from the monolayer in Fig. 6(a) to the bilayer Fig. 6(d). Our results in $\vec{a}$-direction are consistent with the experimental values, but a little smaller than that of the experimental values in $\vec{b}$-direction. This limited discrepancy is probably derived from the layer-dependent effect. In the experiment, the investigated samples are more two layers of As_2S_3, while our calculation is exactly the bilayer system [1]. However, both the experimental data and our calculated results confirm the high anisotropic mechanical properties of 2D As_2S_3 material.

We find that the highly anisotropic mechanical properties in As_2S_3 systems can be explained by As—S—As bond angles along $\vec{a}$-direction. All optimized As—S bond lengths range from 2.28 to 2.31 Å in both monolayer and bilayer As_2S_3, but they have different bond angles. We find that all the As—S—As bond angles can be classified into two types, one is the mainly elongated bonds along with $\vec{a}$-direction, called A-type shown in Figs. 1(a) and 1(b), with A-type bond angles of 89° and 88°, respectively. In contrast, the other As—S—As bond angle is called B-type with a value of 102° and 101° for monolayer and bilayer As_2S_3, separately. The smaller As—S—As bond angle of A-type along $\vec{a}$-direction will enhance the strength of the As—As bonds ($As_1 - As_2$ in Fig. 1 and S—S bonds ($S_1 - S_2$ in Fig. 1(a)). However, the bond angles of the B-type result in the weakness of As—As bonds ($As_1 - As_3$ in Fig. 1 and S—S bonds ($S_2 - S_3$ in Fig. 1(a)) along $\vec{b}$-direction. As a consequence, large anisotropic Young's modulus E and ν are identified and verified.

4. Conclusions

In this work, we have systematically explored the charge distribution, electronic band structures, angle-resolved effective masses, mobility, strain–stress curves, orientation-dependent Young's modulus, Poisson's ratio, and Shear modulus for monolayer and bilayer As_2S_3 by first-principles calculations. The result shows that monolayer and bilayer As_2S_3 have significantly large anisotropy of electronic and mechanical properties. The electronic anisotropy would make 2D As_2S_3 a superior candidate for applications in the photovoltaic field where the generated holes and electrons need to be separated. More interestingly, the calculated anisotropic factor of monolayer and bilayer As_2S_3 are 3.15 and 3.32, respectively, which are significantly higher than that of BP, showing a factor of 2. We expect our study will provide valuable guidance for orientation-related nano-devices, as well as for promoting related experimental investigations.

CRediT authorship contribution statement

Xuefei Liu: Investigation, Methodology, Data curation, Visualization, Writing - review & editing. **Zhaofu Zhang:** Software, Visualization. **Zhao Ding:** Visualization, Writing - review & editing. **Bing Lv:** Software, Visualization. **Zijiang Luo:** Investigation, Writing - review & editing. **Jian-Sheng Wang:** Investigation, Methodology, Writing - review & editing. **Zhibin Gao:** Investigation, Conceptualization, Methodology, Writing - review & editing, Project administration.

Declaration of Competing Interest

The authors declare that they have no known competing financial interests or personal relationships that could have appeared to influence the work reported in this paper.

Acknowledgement

This work is supported by the National Natural Science Foundation of China (Grant No. 61564002 and 11664005); Scientific and Technological Cooperation Projects of Guizhou Province, China (Grant No. [2013] 7019). Science and technology planning project of Guizhou province (Grant No. 2017-5736-009). J.-S. Wang and Z. Gao acknowledge the financial support from MOE tier 1 funding of Singapore (Grant No. R-144-000-402–114).

References

[1] M. šiškins, M. Lee, F. Alijani, M.R. van Blankenstein, D. Davidovikj, H.S. van der Zant, P.G. Steeneken, Highly anisotropic mechanical and optical properties of 2d layered as_2s_3 membranes, ACS Nano 13 (2019) 10845–10851. URL https://pubs.acs.org/doi/abs/10.1021/acsnano.9b06161.

[2] J. Tao, W. Shen, S. Wu, L. Liu, Z. Feng, C. Wang, C. Hu, P. Yao, H. Zhang, W. Pang, X. Duan, J. Liu, C. Zhou, D. Zhang, Mechanical and electrical anisotropy of few-layer black phosphorus, ACS Nano 9 (2015) 11362–11370. URL https://pubs.acs.org/doi/abs/10.1021/acsnano.5b05151.

[3] K.S. Novoselov, A.K. Geim, S.V. Morozov, D. Jiang, Y. Zhang, S.V. Dubonos, I. V. Grigorieva, A.A. Firsov, Electric field effect in atomically thin carbon films, Science 306 (2004) 666–669, https://doi.org/10.1126/science.1102896. URL https://science.sciencemag.org/content/306/5696/666.

[4] K.S. Novoselov, A.K. Geim, S.V. Morozov, D. Jiang, M.I. Katsnelson, I. V. Grigorieva, S.V. Dubonos, A.A. Firsov, Two-dimensional gas of massless dirac fermions in graphene, Nature 438 (2005) 197–200, https://doi.org/10.1038/nature04233. URL https://www.nature.com/articles/nature04233.

[5] Y. Lin, J.W. Connell, Advances in 2d boron nitride nanostructures: nanosheets, nanoribbons, nanomeshes, and hybrids with graphene, Nanoscale 4 (2012) 6908–6939, https://doi.org/10.1039/C2NR32201C.

[6] Q.H. Wang, K. Kalantar-Zadeh, A. Kis, J.N. Coleman, M.S. Strano, Electronics and optoelectronics of two-dimensional transition metal dichalcogenides, Nat. Nanotechnol. 7 (2012) 699, https://doi.org/10.1038/nnano.2012.193. URL https://www.nature.com/articles/nnano.2012.193.

[7] Z. Gao, Z. Zhou, D. Tománek, Degenerately doped transition metal dichalcogenides as ohmic homojunction contacts to transition metal dichalcogenide semiconductors, ACS Nano 13 (2019) 5103–5111, https://doi.org/10.1021/acsnano.8b08190. URL https://pubs.acs.org/doi/abs/10.1021/acsnano.8b08190.

[8] C. Chang, M. Wu, D. He, Y. Pei, C.-F. Wu, X. Wu, H. Yu, F. Zhu, K. Wang, Y. Chen, L. Huang, J.-F. Li, J. He, L.-D. Zhao, 3d charge and 2d phonon transports leading to high out-of-plane ZT in n-type snse crystals, Science 360 (2018) 778–783. URL https://science.sciencemag.org/content/360/6390/778.

[9] Z. Zhu, X. Cai, S. Yi, J. Chen, Y. Dai, C. Niu, Z. Guo, M. Xie, F. Liu, J.-H. Cho, Y. Jia, Z. Zhang, Multivalency-driven formation of te-based monolayer materials: A combined first-principles and experimental study, Phys. Rev. Lett. 119 (2017) 106101, https://doi.org/10.1103/PhysRevLett.119.106101. URL https://link.aps.org/doi/10.1103/PhysRevLett.119.106101.

[10] Z. Gao, F. Tao, J. Ren, Unusually low thermal conductivity of atomically thin 2d tellurium, Nanoscale 10 (2018) 12997–13003, https://doi.org/10.1039/C8NR01649F.

[11] H. Liu, A.T. Neal, Z. Zhu, Z. Luo, X. Xu, D. Tománek, P.D. Ye, Phosphorene: an unexplored 2d semiconductor with a high hole mobility, ACS Nano 8 (2014) 4033–4041, https://doi.org/10.1021/nn501226z. URL https://pubs.acs.org/doi/abs/10.1021/nn501226z.

[12] C. Tan, P. Yu, Y. Hu, J. Chen, Y. Huang, Y. Cai, Z. Luo, B. Li, Q. Lu, L. Wang, Z. Liu, H. Zhang, High-yield exfoliation of ultrathin two-dimensional ternary chalcogenide nanosheets for highly sensitive and selective fluorescence dna sensors, J. Am. Chem. Soc. 137 (2015) 10430–10436, https://doi.org/10.1021/jacs.5b06982.

[13] H. Tian, Q. Guo, Y. Xie, H. Zhao, C. Li, J.J. Cha, F. Xia, H. Wang, Anisotropic black phosphorus synaptic device for neuromorphic applications, Adv. Mater. 28 (2016) 4991–4997, https://doi.org/10.1002/adma.201600166.

[14] H. Wang, M.-L. Chen, M. Zhu, Y. Wang, B. Dong, X. Sun, X. Zhang, S. Cao, X. Li, J. Huang, L. Zhang, W. Liu, D. Sun, Y. Ye, K. Song, J. Wang, Y. Han, T. Yang, H. Guo, C. Qin, L. Xiao, J. Zhang, J. Chen, Z. Han, Z. Zhang, Gate tunable giant anisotropic resistance in ultra-thin gate, Nat. Commun. 10 (2019) 1–8, https://doi.org/10.1038/s41467-019-10256-3.

[15] E. Liu, Y. Fu, Y. Wang, Y. Feng, H. Liu, X. Wan, W. Zhou, B. Wang, L. Shao, C.-H. Ho, Y.-S. Huang, Z. Cao, L. Wang, A. Li, J. Zeng, F. Song, X. Wang, Y. Shi, H. Yuan, H.Y. Hwang, Y. Cui, F. Miao, D. Xing, Integrated digital inverters based on two-dimensional anisotropic res_2 field-effect transistors, Nat. Commun. 6 (2015) 1–7. URL https://www.nature.com/articles/ncomms7991.

[16] H. Yuan, X. Liu, F. Afshinmanesh, W. Li, G. Xu, J. Sun, B. Lian, A.G. Curto, G. Ye, Y. Hikita, Z. Shen, S.-C. Zhang, X. Chen, M. Brongersma, H.Y. Hwang, Y. Cui, Polarization-sensitive broadband photodetector using a black phosphorus vertical

p–n junction, Nat. Nanotechnol. 10 (2015) 707, https://doi.org/10.1038/nnano.2015.112. URL https://www.nature.com/articles/nnano.2015.112.
[17] B. Sa, J. Chen, X. Yang, H. Yang, J. Zheng, C. Xu, J. Li, B. Wu, H. Zhan, Elastic anisotropy and optic isotropy in black phosphorene/transition-metal trisulfide van der waals heterostructures, ACS Omega 4 (2019) 4101–4108, https://doi.org/10.1021/acsomega.9b00011. URL https://pubs.acs.org/doi/abs/10.1021/acsomega.9b00011.
[18] S. Zhao, B. Dong, H. Wang, H. Wang, Y. Zhang, Z.V. Han, H. Zhang, In-plane anisotropic electronics based on low-symmetry 2d materials: progress and prospects, Nanoscale Adv. 2 (2020) 109–139, https://doi.org/10.1039/C9NA00623K.
[19] W. Shen, C. Hu, J. Tao, J. Liu, S. Fan, Y. Wei, C. An, J. Chen, S. Wu, Y. Li, J. Liu, D. Zhang, L. Sun, X. Hu, Resolving the optical anisotropy of low-symmetry 2d materials, Nanoscale 10 (2018) 8329–8337, https://doi.org/10.1039/C7NR09173G. URL https://pubs.rsc.org/en/content/articlelanding/2018/nr/c7nr09173g/unauth.
[20] H. Yang, H. Jussila, A. Autere, H.-P. Komsa, G. Ye, X. Chen, T. Hasan, Z. Sun, Optical waveplates based on birefringence of anisotropic two-dimensional layered materials, ACS Photon. 4 (2017) 3023–3030. URL https://pubs.acs.org/doi/abs/10.1021/acsphotonics.7b00507.
[21] X. Zhou, X. Hu, B. Jin, J. Yu, K. Liu, H. Li, T. Zhai, Highly anisotropic gese nanosheets for phototransistors with ultrahigh photoresponsivity, Adv. Sci. 5 (2018) 1800478. URL https://onlinelibrary.wiley.com/doi/full/10.1002/advs.201800478.
[22] M.N. Ali, J. Xiong, S. Flynn, J. Tao, Q.D. Gibson, L.M. Schoop, T. Liang, N. Haldolaarachchige, M. Hirschberger, N.P. Ong, R.J. Cava, Large, non-saturating magnetoresistance in wte_2, Nature 514 (2014) 205–208. URL https://www.nature.com/articles/nature13763.
[23] G. Qiu, S. Huang, M. Segovia, P.K. Venuthurumilli, Y. Wang, W. Wu, X. Xu, P.D. Ye, Thermoelectric performance of 2d tellurium with accumulation contacts, Nano Lett. 19 (2019) 1955–1962, https://doi.org/10.1021/acs.nanolett.8b05144.
[24] Y. Yin, C. Shao, C. Zhang, Z. Zhang, X. Zhang, J. Robertson, Y. Guo, The anisotropic transport property of antimonene mosfets, ACS Appl. Mater. Interfaces 12 (2020) 22378–22386, https://doi.org/10.1021/acsami.0c04662.
[25] Q. Wei, X. Peng, Superior mechanical flexibility of phosphorene and few-layer black phosphorus, Appl. Phys. Lett. 104 (2014) 251915, https://doi.org/10.1063/1.4885215.
[26] A. Castellanos-Gomez, L. Vicarelli, E. Prada, J.O. Island, K.L. Narasimha-Acharya, S.I. Blanter, D.J. Groenendijk, M. Buscema, G.A. Steele, J.V. Alvarez, H. W. Zandbergen, J.J. Palacios, H.S.J. van der Zant, Isolation and characterization of few-layer black phosphorus, 2D Mater. 1 (2014) 025001. URL https://iopscience.iop.org/article/10.1088/2053-1583/1/2/025001/meta.
[27] J.P. Perdew, K. Burke, M. Ernzerhof, Generalized gradient approximation made simple, Phys. Rev. Lett. 77 (1996) 3865–3868, https://doi.org/10.1103/PhysRevLett.77.3865. URL https://link.aps.org/doi/10.1103/PhysRevLett.77.3865.
[28] G. Kresse, J. Furthmüller, Efficient iterative schemes for Ab Initio total-energy calculations using a plane-wave basis set, Phys. Rev. B 54 (1996) 11169–11186, https://doi.org/10.1103/PhysRevB.54.11169. URL https://link.aps.org/doi/10.1103/PhysRevB.54.11169.
[29] G. Kresse, J. Furthmüller, Efficiency of ab-initio total energy calculations for metals and semiconductors using a plane-wave basis set, Comput. Mater. Sci. 6 (1996) 15–50, https://doi.org/10.1016/0927-0256(96)00008-0. URL http://www.sciencedirect.com/science/article/pii/0927025696000080.
[30] S. Grimme, Semiempirical gga-type density functional constructed with a long-range dispersion correction, J. Comput. Chem. 27 (2006) 1787–1799. URL https://onlinelibrary.wiley.com/doi/abs/10.1002/jcc.20495.
[31] J. Heyd, G.E. Scuseria, M. Ernzerhof, Hybrid functionals based on a screened coulomb potential, J. Chem. Phys. 118 (2003) 8207–8215, https://doi.org/10.1063/1.1564060.
[32] V. Wang, N. Xu, J.-C. Liu, G. Tang, W.-T. Geng, Vaspkit: A pre-and post-processing program for vasp code, arXiv: 1908 (2019) 08269. URL https://arxiv.org/abs/1908.08269.
[33] X. Liu, B. Lv, Z. Ding, Z. Luo, External uniaxial compressive strain induced built-in electric field in bilayer two-dimensional as2s3 for photocatalytic water splitting: A first-principles study, Appl. Surf. Sci. 535 (2021) 147701, https://doi.org/10.1016/j.apsusc.2020.147701. URL http://www.sciencedirect.com/science/article/pii/S0169433220324582.
[34] M. Frumar, A. Firth, A. Owen, Optically induced crystal-to-amorphous-state transition in as2s3, J. Non-Cryst. Solids 192–193 (1995) 447–450, https://doi.org/10.1016/0022-3093(95)00426-2, structure of Non-Crystalline Materials 6. URL http://www.sciencedirect.com/science/article/pii/0022309395004262.
[35] B. Mortazavi, F. Shojaei, M. Azizi, T. Rabczuk, X. Zhuang, as_2s_3, as_2se_3 and as_2te_3 nanosheets: superstretchable semiconductors with anisotropic carrier mobilities and optical properties, J. Mater. Chem. C 8 (2020) 2400–2410, https://doi.org/10.1039/C9TC05904K.
[36] G. Henkelman, A. Arnaldsson, H. Jónsson, A fast and robust algorithm for bader decomposition of charge density, Comput. Mater. Sci. 36 (2006) 354–360. URL https://www.sciencedirect.com/science/article/abs/pii/S0927025605001849.
[37] B. Silvi, A. Savin, Classification of chemical bonds based on topological analysis of electron localization functions, Nature 371 (1994) 683–686. URL https://www.nature.com/articles/371683a0.
[38] Z. Gao, G. Liu, J. Ren, High thermoelectric performance in two-dimensional tellurium: An ab initio study, ACS Appl. Mater. Interfaces 10 (2018) 40702–40709, https://doi.org/10.1021/acsami.8b11836.
[39] R. Nelson, C. Ertural, J. George, V.L. Deringer, G. Hautier, R. Dronskowski, Lobster: Local orbital projections, atomic charges, and chemical-bonding analysis from projector-augmented-wave-based density-functional theory, J Comput Chem 41 (2020) 1931–1940, https://doi.org/10.1002/jcc.26353. URL https://www.ncbi.nlm.nih.gov/pubmed/32531113.
[40] W. Zhou, N. Umezawa, Insight into the band structure engineering of single-layer sns2 with in-plane biaxial strain, PCCP 18 (2016) 7860–7865, https://doi.org/10.1039/c6cp00039h.
[41] L. Wang, L. Huang, W.C. Tan, X. Feng, L. Chen, X. Huang, K.-W. Ang, 2d photovoltaic devices: progress and prospects, Small Methods 2 (2018) 1700294. URL https://onlinelibrary.wiley.com/doi/abs/10.1002/smtd.201700294.
[42] M.S. Dresselhaus, G. Chen, M.Y. Tang, R. Yang, H. Lee, D. Wang, Z. Ren, J.-P. Fleurial, P. Gogna, New directions for low-dimensional thermoelectric materials, Adv. Mater. 19 (2007) 1043–1053, https://doi.org/10.1002/adma.200600527.
[43] J.P. Heremans, V. Jovovic, E.S. Toberer, A. Saramat, K. Kurosaki, A. Charoenphakdee, S. Yamanaka, G.J. Snyder, Enhancement of thermoelectric efficiency in pbte by distortion of the electronic density of states, Science 321 (2008) 554–557. URL https://science.sciencemag.org/content/321/5888/554.
[44] J. Bardeen, W. Shockley, Deformation potentials and mobilities in non-polar crystals, Phys. Rev. 80 (1950) 72–80, https://doi.org/10.1103/PhysRev.80.72. URL https://link.aps.org/doi/10.1103/PhysRev.80.72.
[45] J. Qiao, X. Kong, Z.-X. Hu, F. Yang, W. Ji, High-mobility transport anisotropy and linear dichroism in few-layer black phosphorus, Nature Commun. 5 (2014) 4475, https://doi.org/10.1038/ncomms5475.
[46] G.N. Greaves, A. Greer, R.S. Lakes, T. Rouxel, Poisson's ratio and modern materials, Nat. Mater. 10 (2011) 823–837, https://doi.org/10.1038/nmat3134.
[47] Z. Gao, X. Dong, N. Li, J. Ren, Novel two-dimensional silicon dioxide with in-plane negative poisson's ratio, Nano Lett. 17 (2017) 772–777, https://doi.org/10.1021/acs.nanolett.6b03921.
[48] Z. Gao, D. Liu, D. Tománek, Two-dimensional mechanical metamaterials with unusual poisson ratio behavior, Phys. Rev. Applied 10 (2018) 064039, https://doi.org/10.1103/PhysRevApplied.10.064039. URL https://link.aps.org/doi/10.1103/PhysRevApplied.10.064039.
[49] V. Wang, W. Geng, Lattice defects and the mechanical anisotropy of borophene, J. Phys. Chem. C 121 (2017) 10224–10232. URL https://pubs.acs.org/doi/abs/10.1021/acs.jpcc.7b02582.
[50] R.C. Andrew, R.E. Mapasha, A.M. Ukpong, N. Chetty, Mechanical properties of graphene and boronitrene, Phys. Rev. B 85 (2012) 125428. URL https://journals.aps.org/prb/abstract/10.1103/PhysRevB.85.125428.
[51] C. Jasiukiewicz, T. Paszkiewicz, S. Wolski, Auxetic properties and anisotropy of elastic material constants of 2d crystalline media, Phys. Status Solidi B 245 (2008) 562–569. URL https://onlinelibrary.wiley.com/doi/abs/10.1002/pssb.200777713.
[52] C. Jasiukiewicz, T. Paszkiewicz, S. Wolski, Auxetic properties and anisotropy of elastic material constants of 2d crystalline media [phys. status solidi b 245, no. 3, 562–569 (2008)], Phys. Status Solidi B 247 (2010), 1247–1247, https://onlinelibrary.wiley.com/doi/full/10.1002/pssb.200945615.